Planform selection in Bénard-Marangoni convection: *l* hexagons versus *g* hexagons

A. Thess[1] and M. Bestehorn[2]
[1]*Institut für Strömungsmechanik, Technische Universität Dresden, 01062 Dresden, Germany*
[2]*Institut für Theoretische Physik und Synergetik, Universität Stuttgart, Pfaffenwaldring 57/4, 70550 Stuttgart, Germany*
(Received 2 May 1995)

The planform of weakly nonlinear Bénard-Marangoni convection in a horizontally unbounded layer is analyzed using a combination of direct numerical simulation, amplitude equations, and qualitative discussion. It is demonstrated that there exists a critical Prandtl number Pr_c such that in fluids with $\mathrm{Pr}<\mathrm{Pr}_c$ convection sets in as a pattern of hexagonal cells with downward motion in the center (*g* hexagons), while for fluids with $\mathrm{Pr}>\mathrm{Pr}_c$ conventional hexagonal cells with upward motion in the center (*l* hexagons) appear at the onset of instability. For fluids with Marangoni and Prandtl numbers in the vicinity of the bicritical point $(\mathrm{Ma}_c,\mathrm{Pr}_c)$ the hexagonal patterns undergo a secondary instability, leading to stationary rolls. The stability domain of stationary rolls increases with the distance from the critical Marangoni number.

PACS number(s): 47.20.Dr, 47.20.Ky, 47.32.Cc

I. INTRODUCTION AND BASIC EQUATIONS

After the pioneering work of Bénard [1], Block [2], and Pearson [3], surface tension driven convection in a fluid layer heated from below ("Bénard-Marangoni convection" or BMC) has received considerable attention and is now reasonably well understood [4–7], as far as fluids with *high* Prandtl number are concerned. In particular, the universality of the hexagonal planform of weakly nonlinear convection has been unambiguously demonstrated both experimentally [4] and theoretically [6,7]. In contrast, virtually nothing is known about Bénard-Marangoni convection in *low*-Prandtl-number fluids. The only experimental study of low-Prandtl-number BMC is that of Ginde, Gill, and Verhoeven [8], which has been performed with liquid tin ($\mathrm{Pr}=0.017$). Although this experiment has verified the predictions of linear stability theory [3], no visual observation was reported about the planform of convection. On the theoretical side, there is no prediction for fluids with $\mathrm{Pr}\ll 1$ that goes beyond linear stability analysis or asymptotic bifurcation theory [9,10].

The goal of the present paper is to report direct numerical simulations of the weakly nonlinear Bénard-Marangoni problem which, for the first time, extend into the range of low Prandtl number Pr. Moreover, we wish to present an example where the predictions of a weakly nonlinear theory, based on amplitude equations, are directly tested against the results of numerical simulation of the fully time-dependent three-dimensional hydrodynamic problem. After the formulation of the basic equations we shall, in Sec. II, present numerical evidence that in the limit $\mathrm{Pr}\to 0$ the convective planform is still hexagonal but, in contrast to BMC at high Prandtl number, consists of cells with *downward* rather than upward fluid motion in the center. In Sec. III we predict, using amplitude equations, that this type of cell should be observed for fluids with $0<\mathrm{Pr}<\mathrm{Pr}_c$ where the critical Prandtl number depends only weakly on the thermal conditions at the free surface expressed by the Biot number. Section IV contains the results of a series of direct numerical simulations performed in order to test quantitatively the weakly nonlinear theory. Finally, in Sec. V, we wish to explain the reason for the selection of different hexagon types in terms of simple fluid-dynamical principles.

Our investigation is based on the following set of dimensionless equations

$$\mathrm{Pr}^{-1}\{\partial_t\mathbf{v}+(\mathbf{v}\cdot\nabla)\mathbf{v}\}=-\nabla p+\nabla^2\mathbf{v}\ , \tag{1}$$

$$\nabla\cdot\mathbf{v}=0\ , \tag{2}$$

$$\partial_t\theta+(\mathbf{v}\cdot\nabla)\theta=v_z+\nabla^2\theta\ , \tag{3}$$

with the boundary conditions

$$v_x=v_y=v_z=\theta=0\quad\text{for } z=0\ , \tag{4}$$

$$\partial_z v_x+\mathrm{Ma}\partial_x\theta=\partial_z v_y+\mathrm{Ma}\partial_y\theta=v_z=0\ , \tag{5a}$$

$$\partial_z\theta+\mathrm{Bi}\theta=0\quad\text{for } z=1\ , \tag{5b}$$

and with periodic boundary conditions $\mathbf{v}(x+l_x,y+l_y,z)=\mathbf{v}(x,y,z),\theta(x+l_x,y+l_y,z)=\theta(x,y,z)$ in the horizontal directions. They describe the velocity $\mathbf{v}(\mathbf{x},t)$, pressure $p(\mathbf{x},t)$, and temperature $T(\mathbf{x},t)=T_0-z+\theta(\mathbf{x},t)$ in a fluid layer, which is heated from below and which is characterized by its depth d, applied temperature difference ΔT, density ρ, kinematic viscosity ν, heat diffusivity κ, and temperature coefficient of surface tension γ. Space, time, velocity, pressure and temperature are measured respectively in units of d, d^2/κ, κ/d, $\rho\nu\kappa/d^2$, and ΔT. Equations (1)–(5) contain five dimensionless parameters, namely, the Marangoni number $\mathrm{Ma}=\gamma d\Delta T/\rho\nu\kappa$, which measures the strength of the basic temperature gradient, the Prandtl number $\mathrm{Pr}=\nu/\kappa$, which is a property of the fluid, the Biot number $\mathrm{Bi}=\alpha d/\lambda$ [11], which characterizes the heat loss at

the free surface, and the aspect ratios l_x and l_y. The derivation and discussion of (1)–(5), in which the influence of buoyancy and surface deflection has been neglected, can be found, e.g., in Ref. [12].

It is known from linear stability theory [3] that for $\mathrm{Ma}_c \approx 79.606$ (at $\mathrm{Bi}=0$) the quiescent solution $\mathbf{v}=p=\theta=0$ of the governing equations becomes unstable with respect to infinitesimal spatially periodic perturbations with wave number $k=1.99$. While the threshold $\mathrm{Ma}_c(\mathrm{Bi})$ and the critical wave number $k_c(\mathrm{Bi})$ of this Bénard-Marangoni instability do not depend on the Prandtl number, the nonlinear evolution following the primary instability is strongly influenced by this parameter, as will be shown below. In what follows we shall confine our attention to the weakly nonlinear regime, which is mathematically expressed by the condition $\varepsilon=(\mathrm{Ma}-\mathrm{Ma}_c)/\mathrm{Ma}_c \ll 1$.

Parmentier, Regnier, and Lebon [13] have also performed work similar to the present one, in which the existence of g hexagons in low-Prandtl-number convection has been predicted using amplitude equations.

II. NUMERICAL EXPERIMENTS FOR $\mathrm{Pr}\to\infty$ AND $\mathrm{Pr}\to 0$

A useful key to the understanding of Bénard-Marangoni convection comes through elucidation of the limits $\mathrm{Pr}\to\infty$ and $\mathrm{Pr}\to 0$, in which the governing equations can be greatly reduced to the following two conceptually simple models.

Infinite Prandtl-number convection, which is an approximation to the behavior of very viscous fluids like silicone oil, is characterized by small Reynolds number $\mathrm{Re}=vd/\nu$ (v is a characteristic velocity) and by the smallness of the viscous diffusion time d^2/ν in comparison to the thermal diffusion time d^2/κ. This results in the hydrodynamic part of the problem being governed by the linear Stokes equation instead of the nonlinear Navier-Stokes equation (1) (cf. Refs. [6] and [7]). Thus, the infinite Prandtl-number model takes the form

$$\mathbf{0}=-\nabla p+\nabla^2\mathbf{v}\ , \tag{6a}$$

$$\partial_t\theta+(\mathbf{v}\cdot\nabla)\theta=v_z+\nabla^2\theta\ , \tag{6b}$$

supplemented by (2), (4), and (5).

Low-Prandtl-number fluids such as liquid metals (mercury, gallium, tin) or semiconductor melts are characterized by high heat diffusivity and low viscosity. They differ from high-Prandtl-number fluids in that the Peclet number $\mathrm{Pe}=vd/\kappa$ is small in the weakly nonlinear regime rather than the Reynolds number and in that the thermal equilibration proceeds much faster than viscous decay of perturbations. As pointed out by Thual [14] for Rayleigh-Bénard convection, the limit $\mathrm{Pr}\to 0$ (or $\kappa\to\infty$) can be described by the simplified zero-Prandtl-number model

$$\partial_t\mathbf{v}+(\mathbf{v}\cdot\nabla)\mathbf{v}=-\nabla p+\nabla^2\mathbf{v}\ , \tag{7a}$$

$$0=v_z+\nabla^2\theta\ . \tag{7b}$$

The derivation of these equations requires a scaling of the physical quantities, which differs from the scaling leading to Eqs. (1)–(6). Indeed, taking the limit $\mathrm{Pr}\to 0$ in Eq. (1) does not yield a meaningful result because the scales of time and velocity used for the derivation of the governing equations become singular in the zero-Prandtl-number limit $\kappa\to\infty$. As detailed in [14], d, d^2/ν, ν/d, $\rho\nu^2/d^2$, and $(\nu/\kappa)\Delta T$ are now the appropriate scales of space, time, velocity, pressure, and temperature, which lead to the equations given above. The zero-Prandtl-number model comprises the full Navier-Stokes equation, implying the possibility of small-scale velocity structures and even turbulence. The rudimentary heat equation (7b) describes the instantaneous deformation of the temperature isolines due to the interaction of the vertical velocity component with the mean temperature gradient. From the mathematical viewpoint, zero-Prandtl-number convection is a Navier-Stokes flow with a linear nonlocal feedback mechanism. Indeed, the velocity field immediately creates a temperature perturbation governed by Eq. (7b) which, on account of the Marangoni boundary conditions, Eq. (5a), acts back on the flow field.

We have numerically solved the governing equations for both limiting cases using a pseudospectral method with Fourier series in the horizontal direction and Chebyshev polynomial series in the vertical direction. Details of the infinite-Prandtl-number code are given in Ref. [7]; details of the zero-Prandtl-number code, which differs from the former code by the presence of vertical vorticity, will be reported elsewhere. With a vertical resolution of 32 collocation points both codes reproduce the critical Marangoni number $\mathrm{Ma}_c \approx 79.606$ (at $k=1.99$ and $\mathrm{Bi}=0$) to at least three significant digits. For a horizontal resolution of 128×128 collocation points we can perform either large-aspect-ratio simulations (e.g., $l_x=l_y=20$) for weakly supercritical Marangoni numbers (e.g., $\mathrm{Ma}=80$) or small-aspect-ratio simulations for high Marangoni numbers [7]. The advantage of a fully numerical simulation is that no *a priori* restriction is imposed on the pattern apart from the finite aspect ratio.

As an additional diagnostic we can perturbatively compute the deflection of the free surface from the velocity field obtained in the code with nondeflecting surface. To zero order in the surface deflection $h(x,y,t)$ the normal velocity obeys the boundary condition $v_z=0$. The first-order surface deflection is related to the zero-order velocity and pressure by the linearized normal stress boundary condition

$$\rho g h-\sigma\Delta h=p-2\rho\nu\partial_z v_z \tag{8}$$

(see, e.g., [15]) where v_z and p are dimensional quantities and g and σ denote the acceleration of gravity and the surface tension, respectively. Introducing Fourier-transformed quantities $\hat{h}$, $\hat{p}$, and $\hat{v}_z$, the horizontal wave number k, and measuring the surface deflection in units of d, Eq. (8) can be recast in the following form

$$\hat{h}=f(k)(2\partial_z\hat{v}_z-\hat{p})\ , \tag{9}$$

where $\hat{p}$ and $\hat{v}_z$ are nondimensional variables and $f(k)=\rho\kappa\nu/(\rho g d^3+\sigma d k^2)$ for the finite-Prandtl-number scaling and $f(k)=\rho\nu^2/(\rho g d^3+\sigma d k^2)$ for the zero-

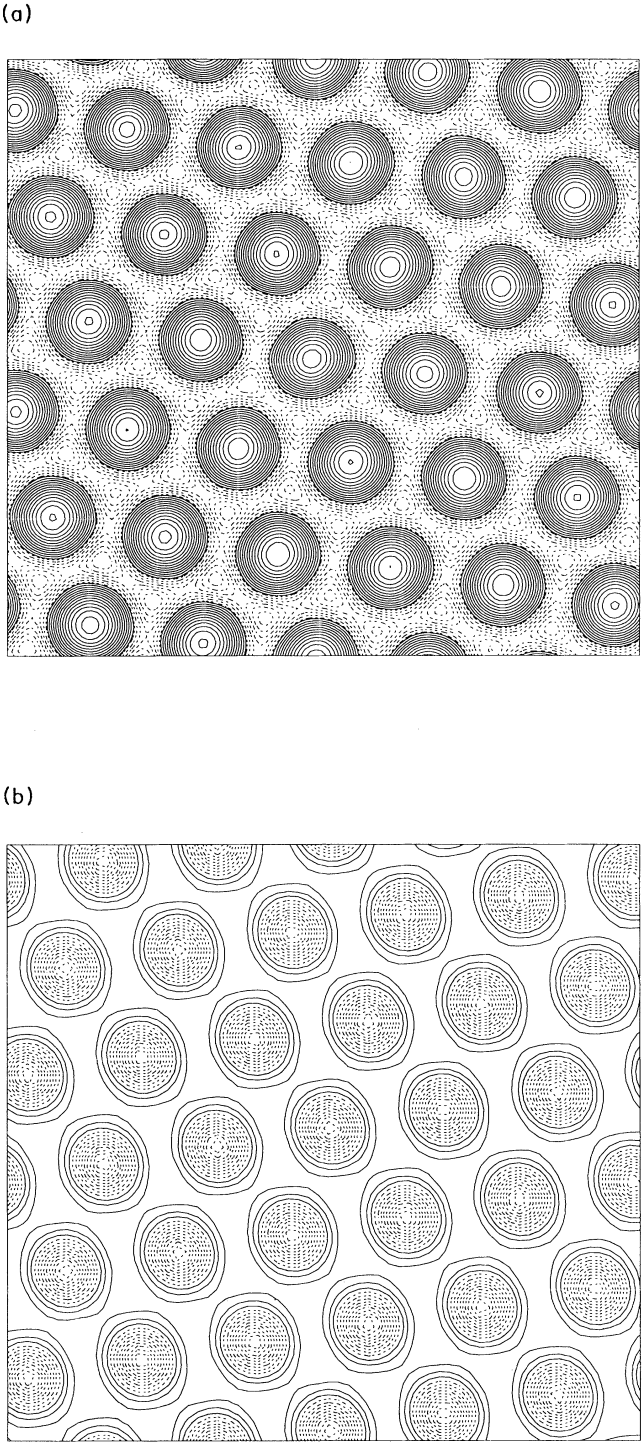

FIG. 1. l hexagons vs g hexagons in Bénard-Marangoni convection: Surface temperature fields for Ma=80 evolving from random initial conditions in a fluid with (a) infinite Prandtl number and (b) zero Prandtl number. Aspect ratios are $l_x=l_y=20$, spatial resolution is $128\times128\times32$, Bi=0. Solid lines correspond to positive, dashed lines to negative values of surface temperature.

Prandtl-number scaling. When the zero-order velocity and pressure fields are known at the free surface, as is the case in our numerical simulation, the first-order surface deflection can be explicitly computed from Eq. (9). Notice, however, that in addition to Ma, Bi, l_x, and l_y, the parameters g and σ have to be specified in order to make quantitative predictions for h. Since a systematic study of the influence of gravity and surface tension is outside the scope of the present paper, we only use $2\partial_z v_z - p$ as a qualitative diagnostic for the *shape* of the free surface.

In Fig. 1 we plot two surface temperature fields that have evolved from random initial conditions under infinite Prandtl number [Eqs. (2), (4), (5), and (6)] and under zero Prandtl number [Eqs. (2), (4), (5) and (7)]. The hexagonal pattern of the infinite-Prandtl-number case [Fig. 1(a)] has already been described in detail in Refs. [6,7] and is reproduced here for the purpose of comparing it with the result of the zero-Prandtl-number convection, plotted in Fig. 1(b). Apparently, the latter flow is a hexagonal lattice of convective cells as in the infinite-Prandtl-number case. However, cold fluid flows *downward* in the center of the cells in contrast to the infinite-Prandtl-number case [Fig. 1(a)] where the cells are formed by warm *upflowing* fluid. The deformed fluid surface is found to be convex over the downflowing (cold) regions as is expected in surface tension driven convection. "Inverted" hexagons of the type plotted in Fig. 1(b) are known to exist in gases. They have been termed "g [gas] hexagons" in contrast to the more familiar "l [liquid] hexagons" [16]. Our simulation demonstrates that the existence of g hexagons is not necessarily related to non-Boussinesq effects, which are responsible for their formation in gases. Convective cells with downward flow in the center have been predicted for low-Prandtl-number BMC in laterally bounded domains by Rosenblat, Davis, and Homsy [9] and later by Dauby *et al.* [10] using bifurcation theory. The present result appears to be the first fully numerical verification of these predictions.

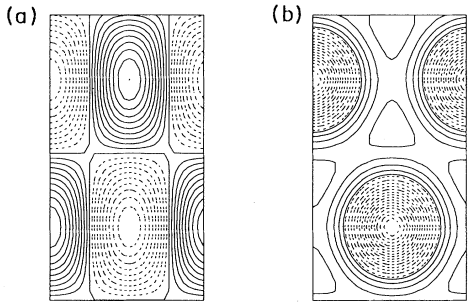

FIG. 2. Planform selection in zero-Prandtl-number convection: Surface temperature field of (a) initial condition and (b) the final stationary state for Ma=80. Aspect ratios are $l_x=4\pi/\sqrt{3}\approx7.26$ and $l_y=4\pi\approx12.6$, spatial resolution is $64\times64\times32$, Bi=0. Solid lines correspond to positive, dashed lines to negative values of surface temperature.

In order to verify the robustness of g hexagons, we have performed several zero-Prandtl-number simulations using deterministic initial conditions and a domain that allows for a perfectly hexagonal cell. First we have used the initial condition plotted in Fig. 2(a), which favors neither g hexagons nor l hexagons. As shown in Fig. 2(b), a stationary g hexagon is formed as a result of the nonlinear evolution affirming the generality of the previous numerical results. In a second simulation we have compared the flow evolving from a g hexagon with the flow evolving from an l hexagon when both initial conditions have the same total kinetic energy, slightly higher than the kinetic energy of the stationary state in Fig. 2(b). While the amplitude of the g hexagon decreases slightly and settles at its stationary value, the amplitude of the l hexagon decreases rapidly to a very small value without the tendency to settle at a metastable state. Finally, as a result of small numerical perturbations and of the primary instability, the flow reorganizes into a g hexagon, grows, and attains the stationary state of Fig. 2(b). The stability of g hexagons is not changed if the foregoing computations are repeated with nonzero values of the Biot number.

After having identified two different types of hexagons in BMC, it is natural to expect that there exists a finite Prandtl number Pr_c at which g hexagons are transformed into l hexagons. There is, in principle, no conceptual or technical difficulty in determining Pr_c entirely within the framework of direct numerical simulation as will be shown in Sec. IV. However, we can demonstrate that a weakly nonlinear analytic theory is capable of providing a first approximation to this value with less computational expense.

III. AMPLITUDE EQUATIONS FOR ARBITRARY PRANDTL NUMBER

Near threshold of convection, a perfect hexagonal pattern can be approximated by a superposition of three cosine functions (see, e.g., [6]). The temperature field can be written as

$$\theta(x,y,z,t)=g(z)\sum_{i=1}^{3}\xi_i(t)\cos(\mathbf{k}_i\cdot\mathbf{x}_\perp)\ , \tag{10}$$

where $\mathbf{x}_\perp$ denotes the horizontal coordinates (x,y) and the $\mathbf{k}_i$ all have the same length $|\mathbf{k}_i|=k_c$ and form a horizontal tristar

$$\sum_{i=1}^{3}\mathbf{k}_i=\mathbf{0}\ . \tag{11}$$

The (positive definite) function $g(z)$ is obtained from the linearized equations (1)–(5). Using this expansion, one may derive amplitude equations for ξ_i, which was first shown in Ref. [17]. Up to cubic order they read

$$\dot{\xi}_1=\tilde{\varepsilon}\xi_1+A\xi_2^*\xi_3^*-[B(|\xi_2|^2+|\xi_3|^2)+C|\xi_1|^2]\xi_1 \tag{12}$$

and cyclic in ξ_2,ξ_3. Here, $B,C>0$ and $\tilde{\varepsilon}\propto\varepsilon$ due to a different scaling. The coefficients A, B, and C result from the eigensolutions of the linearized hydrodynamic equations (1)–(5) and can be found numerically for the case of BMC as demonstrated in Refs. [6,18]. For finite Prandtl number it turns out that A is composed of two parts:

$$A=A_\theta+\frac{1}{\mathrm{Pr}}A_v\ , \tag{13}$$

where A_θ stems from the nonlinearity of the heat equation (3) and A_v from that of the Navier-Stokes equation (1). For closed upper surface (Rayleigh-Bénard convection), A vanishes for symmetry reasons and the cubic terms in (12) usually select rolls. For a nonzero quadratic term, stability analysis shows that at onset ($\varepsilon=0$) hexagons are always the preferred stable planform, namely, l hexagons for $A>0$ and g hexagons for $A<0$. It is clear that the condition $A=0$ yields the Prandtl number for the transition from g hexagons to l hexagons:

$$\mathrm{Pr}_c=-\frac{A_v(\mathrm{Bi})}{A_\theta(\mathrm{Bi})}\ . \tag{14}$$

We evaluated (14) numerically for several Biot numbers. We used a finite-difference method to obtain the z dependence of the eigenfunctions for the linearized problem and to compute the coefficient A. This is a straightforward extension of the algorithm used for infinite Pr and described in detail in [6]. The results are shown in Fig. 3. For the situation in the experiments, where the Biot number tends to zero, we obtain $\mathrm{Pr}_c\approx 0.22$. Note that $\mathrm{Pr}=0.017$ in the liquid-tin experiments of Ref. [8] is well below the critical Prandtl number predicted by our theory. It is very likely that Ginde, Gill, and Verhoeven [8] would have made the experimental discovery of g hexagons in Bénard convection if they had performed a visual observation of the fluid surface, which unfortunately was not done due to the high technical complexity of the experiment.

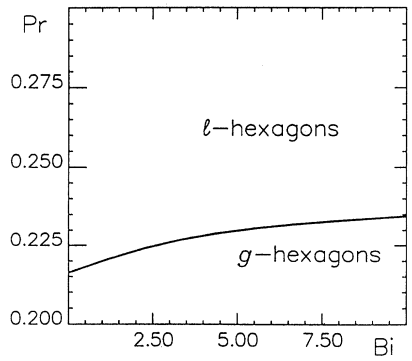

FIG. 3. Critical Prandtl number Pr_c for the transition from l hexagons to g hexagons at threshold ($\varepsilon=0$) for several Biot numbers for purely surface tension driven convection.

IV. DIRECT NUMERICAL SIMULATIONS FOR ARBITRARY PRANDTL NUMBER: A QUANTITATIVE TEST OF THE WEAKLY NONLINEAR THEORY

After having predicted the existence of a bicritical point $(\mathrm{Ma}_c,\mathrm{Pr}_c)$ at which (for $\varepsilon=0$) hexagonal cells change their orientation, we wish to address the following two questions: (1) Is the value of the critical Prandtl number predicted by the weakly nonlinear theory *quantitatively* correct? (2) Which planform is selected in the vicinity of Pr_c for finite values of ε?

A. Hexagons

A regular perfect hexagonal lattice is described by (10) with $\xi_1=\xi_2=\xi_3\equiv\xi$. From (12) it follows for its amplitudes ξ (that we may consider here and in the following without loss of generality as real valued)

$$\dot{\xi}=\bar{\varepsilon}\xi+A\xi^2-(2B+C)\xi^3 . \tag{15}$$

In the following we want to "measure" the coefficients of (15), especially A, by considering stationary numerical solutions of the three-dimensional hydrodynamic equations (1)–(5) for different values of Pr near Pr_c. To integrate the Navier-Stokes equation we used an extension of the numerical code described in [6] that allows us to compute the temporal evolution of the vorticity field. Figure 4 shows the maximum amplitude of a hexagon pattern as a function of Pr. We used a small-aspect-ratio layer with periodic lateral boundary conditions having periodicity lengths $l_x=4\pi/k_c$ and $l_y=4\pi/\sqrt{3}k_c$, allowing for the emergence of one hexagon with the critical wavelength. The integration was continued until the relative change of the temperature field was less than 10^{-5}. For a stationary solution, (15) may be written as

$$0=\bar{\varepsilon}+\gamma(\mathrm{Pr}-\mathrm{Pr}_c)\xi-\xi^2 \tag{16}$$

with $\bar{\varepsilon}=\tilde{\varepsilon}/(2B+C)$. Here we assumed that A depends linearly on $\mathrm{Pr}-\mathrm{Pr}_c$ which is justified for Pr in the vicinity of Pr_c. To determine the unknown coefficients $\bar{\varepsilon}$, γ, and Pr_c from the simulations, we insert the numerically determined values $\xi(\mathrm{Pr})$ into (16) and minimize the residual

$$R(c_1,c_2,c_3)=\int\{c_1+(c_2\mathrm{Pr}-c_3)\xi(\mathrm{Pr})-[\xi(\mathrm{Pr})]^2\}^2 d\,\mathrm{Pr} . \tag{17}$$

This leads to a linear system of three equations $\partial R/\partial c_i=0$ $(i=1\cdots3)$ determining the desired parameters as $\bar{\varepsilon}=c_1$, $\gamma=c_2$, and $\mathrm{Pr}_c=c_3/c_2$. With this procedure we determined $\mathrm{Pr}_c\approx0.29$ for $\mathrm{Bi}=0.1$, in reasonable agreement with the result $\mathrm{Pr}_c(0.1)\approx0.22$. Figure 4 shows also solutions of (16) using the obtained coefficients (dashed line) for the regions below as well as above Pr_c. Notice that the amplitude of the hexagons would experience a jump across Pr_c (cf. the insets in Fig. 4) if hexagons were stable solutions close to critical Prandtl number. This, however, is not the case, as will be shown next.

B. Rolls

For Pr in the direct vicinity of Pr_c, hexagons are unstable and give way to rolls, in agreement with earlier results [16]. Linear stability analysis around hexagons [18]

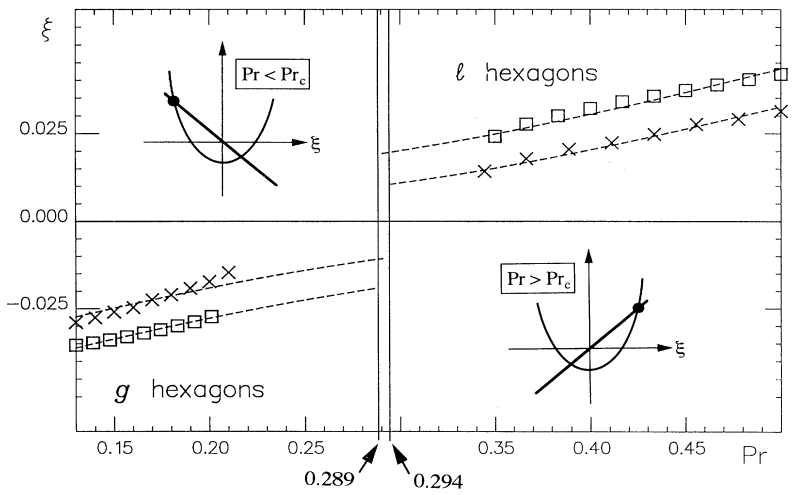

FIG. 4. Hexagon amplitudes obtained by numerical integration of the Navier-Stokes equations in a small-aspect-ratio domain for $\varepsilon=0.01$ (squares) and $\varepsilon=0.0075$ (crosses) with $\mathrm{Bi}=0.1$ and $\mathrm{Ma}_c\approx80$. Minimization of (17) yields the coefficients of the amplitude equation (16). We determined Pr_c for the transition from l hexagons to g hexagons as $\mathrm{Pr}_c=0.294$ (for $\varepsilon=0.0075$) and $\mathrm{Pr}_c=0.289$ (for $\varepsilon=0.01$). The dashed lines show the hexagon amplitudes reconstructed from (16). Insets illustrate the jump of ξ in the vicinity of Pr_c. Sketched are the curves $\xi^2-\bar{\varepsilon}$ and $\gamma(\mathrm{Pr}\text{-}\mathrm{Pr}_c)\xi$ the intersection of which [cf. Eq. (16)] defines the amplitude of the (possibly unstable) hexagon.

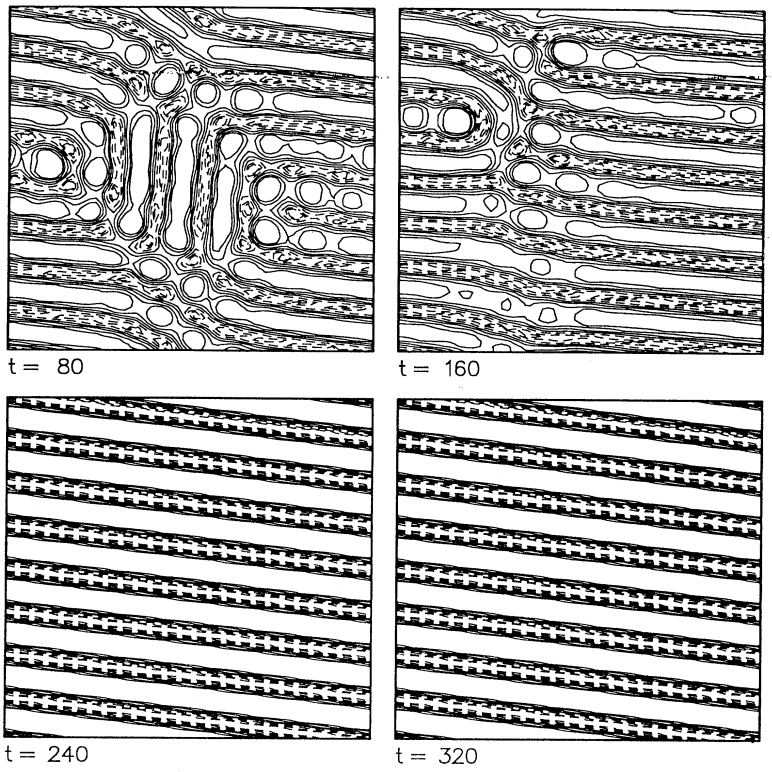

FIG. 5. Spatiotemporal evolution of a large-aspect-ratio system for Pr=0.5, Bi=0.1, random initial conditions, and $\varepsilon=0.13$ in the region (18), where hexagons are unstable. Eventually, parallel steady rolls are formed. Note that the system is still exclusively driven by surface tension. Shown are the contour lines of the temperature field on the top of the layer, solid lines correspond to positive, dashed lines to negative values. The time is measured in units of the vertical heat diffusion.

shows that the size of this region increases with $\sqrt{\varepsilon}$ as

$$\tilde{\gamma}|\mathrm{Pr}-\mathrm{Pr}_c| < \sqrt{\varepsilon} \ , \tag{18}$$

with $\tilde{\gamma}=\gamma(C^2-2B^2+BC)/\sqrt{C}$.

Although possible in principle, it is not an easy task to establish the full set of coupled amplitude equations for a small Prandtl number and to compute all coefficients for the case of BMC. This work is currently in progress. Here we shall continue the discussion for a large-aspect-ratio system (low Pr) by performing again direct numerical solutions of the basic equations. Now we fix the lateral geometry to a unit cell with a rather large aspect ratio $l_x=l_y=16\pi/k_c$, allowing for the occurrence of 8 critical wavelengths in each direction. In this way we are able to obtain a rather complete picture for the formation of several typical structures in the ε-Pr plane. We fixed the Biot number to Bi=0.1 leading to $\mathrm{Ma}_c \approx 80$. For small ε and for Pr inside the range (18) we obtain stable, eventually parallel rolls (Fig. 5). For larger (smaller) Pr outside (18) we obtain stable l (g) hexagons in agreement with the results of Sec. II. From our numerical experiments we estimate the coefficient $\tilde{\gamma}$ of (18) as

$$\tilde{\gamma} \approx 0.9 \ . \tag{19}$$

Figure 6 summarizes the behavior of the system in the vicinity of the critical Prandtl number.

V. PHYSICAL INTERPRETATION

Although we have obtained theoretical evidence for the existence of two different types of hexagons in Bénard-Marangoni convection, the seemingly naive question as to *why* g hexagons (and not l hexagons) are selected for $\mathrm{Pr} \ll 1$ still remains unanswered (as far as physical rather than purely mathematical understanding is desired). We shall attempt to answer this question by providing some physical arguments that highlight dominant nonlinear effects that are markedly different in low- and high-

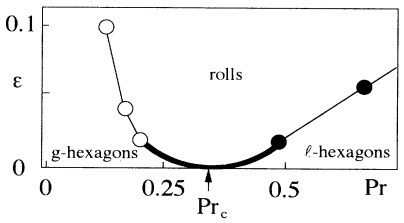

FIG. 6. Phase diagram in the Pr-ε plane. Black (white) circles correspond to transitions from l hexagons (g hexagons) to rolls as determined by direct numerical simulations. The bold parabola show the transition between rolls and hexagons according to the weakly nonlinear theory [Eq. (18) with $\tilde{\gamma}=0.9$]. Thin lines are drawn to guide the eye. The transition curve ε(Pr) is shifted upwards due to the Pr dependence of the cubic coefficient that is not included in (15).

Prandtl-number convection.

According to linear stability theory [3] the fluid becomes unstable with respect to rolls with arbitrary horizontal orientation and, consequently, to any linear superposition of them, including both g and l hexagons, respectively. In order to explain which type of hexagon will be selected, we must examine the nonlinear effects. Our explanation consists of three steps. First we reformulate our problem in terms of production and dissipation of kinetic energy. Second, we illustrate the distinct dominant nonlinear effects for $\mathrm{Pr} \ll 1$ and $\mathrm{Pr} \gg 1$ using a single pair of rolls as a simple prototype. Finally, we consider a single axisymmetric convective cell as an approximation to a hexagonal cell and we argue that the nonlinear effect for the high-Prandtl-number BMC (low-Prandtl-number BMC) acts in such a way that l hexagons (g hexagons) intensify the thermocapillary production of kinetic energy and are therefore favored in the evolution.

The balance between energy production due to surface tension and energy dissipation by viscosity is expressed by the evolution equation

$$\frac{dE}{dt} = -\frac{\gamma}{\rho}\int_S (\mathbf{v}\cdot\nabla)\theta\, dS - \nu\int_V (\nabla\circ\mathbf{v})\cdot(\nabla\circ\mathbf{v})\, dV \quad (20)$$

for the total kinetic energy $E=(\rho/2)\int \mathbf{v}^2 dV$, which is obtained by multiplying Eq. (1) with $\mathbf{v}$, integrating it over the fluid volume V, and making use of the Marangoni boundary conditions [Eq. (5)] at the free surface S. The unstable evolution of a quiescent layer starts with a growth of linearly unstable modes resulting in an exponential increase of the energy. This growth is slowed down by nonlinear deformation of the velocity and temperature fields and finally stops when the stationary state is reached. From the observation of stable g hexagons we can conclude that for $\mathrm{Pr} \ll 1$ the energy production rate in the stationary g hexagon must be higher than in the l hexagon; the latter is not able to overcome viscous energy dissipation in a stable manner. The same argument holds in the case of $\mathrm{Pr} \gg 1$ with the role of g hexagons and l hexagons exchanged. Therefore, the maximization of the thermocapillary energy production rate $-\int(\mathbf{v}\cdot\nabla)\theta\, dS$ can serve as a selection principle.

Consider first the case of high Prandtl number where the dominant nonlinear effect lies in the deformation of temperature isolines described by Eq. (6b) while the hydrodynamic part of the problem is governed by the linear Stokes equation (6a). Figures 7(a) and 7(b) illustrate how an initially symmetric pair of rolls is modified by such nonlinearity. The redistribution of temperature arises from an advection of the temperature isolines and, as a consequence of the source term in Eq. (3), from a growth of the warm region at the expense of the cold region. The result of the nonlinear evolution is sketched in Fig. 7(b) together with the surface temperature field derived from a full numerical simulation at high Marangoni number [Fig. 7(c)]. With these two-dimensional considerations in mind we can proceed to a qualitative analysis of the three-dimensional problem. Instead of considering a single hexagon, it is useful to discuss a slightly modified flow consisting of a single axisymmetric cell enclosed in a circular box. This modification allows us to simplify the integrals in (20). How does the nonlinear redistribution of the temperature affect the thermocapillary energy production in an "l cell" and in a "g cell," respectively? Due to axisymmetry, the first term on the right-hand side of Eq. (20) can be written as

$$-2\pi\frac{\gamma}{\rho}\int_S v_r \frac{\partial\theta}{\partial r} r\, dr\ . \quad (21)$$

Since large-aspect-ratio BMC is driven by local temperature gradients, we can use the estimate $v_r \sim -\partial\theta/\partial r$ in order to express the integral entirely in terms of the surface temperature. The rate of thermocapillary energy production is then found to be proportional to $\int(\partial\theta/\partial r)^2 r\, dr$. Due the weight factor r appearing in the integral, the thermocapillary energy production is intensified when the temperature gradient is advected outward, as in the l hexagon, rather than inward, as in

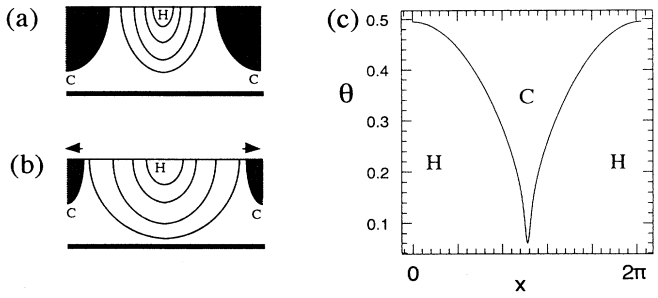

FIG. 7. Illustration of the nonlinear redistribution of temperature in high-Prandtl-number Bénard-Marangoni convection: Sketch of the temperature isolines of a pair of rolls in the (a) weakly nonlinear and in (b) strongly nonlinear regime. Surface temperature field (c) of a deformed roll as obtained from direct numerical simulation of the infinite-Prandtl-number equations for Ma=2000 (aspect ratios $l_x=\pi, l_y=1$, spatial resolution $512\times32\times128$, Bi=0). H and C denote cold and hot regions.

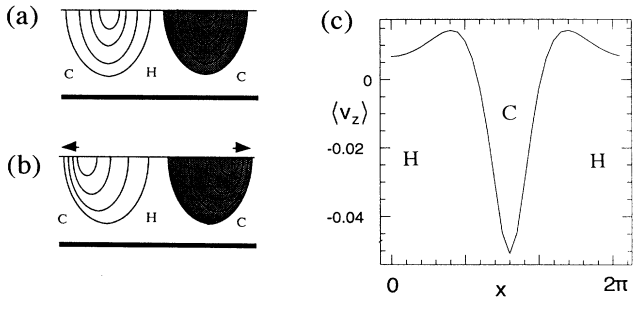

FIG. 8. Illustration of the nonlinear redistribution of vorticity in low-Prandtl-number Bénard-Marangoni convection: Sketch of the vorticity isolines of a pair of rolls in the (a) weakly nonlinear and in (b) strongly nonlinear regime. Velocity averaged over the layer depth (c) of a deformed pair of rolls as obtained from direct numerical simulation of the zero-Prandtl-number equations for Ma=100 (aspect ratios $l_x=\pi, l_y=1$, spatial resolution $64\times32\times64$, Bi=0). H and C denote cold and hot regions.

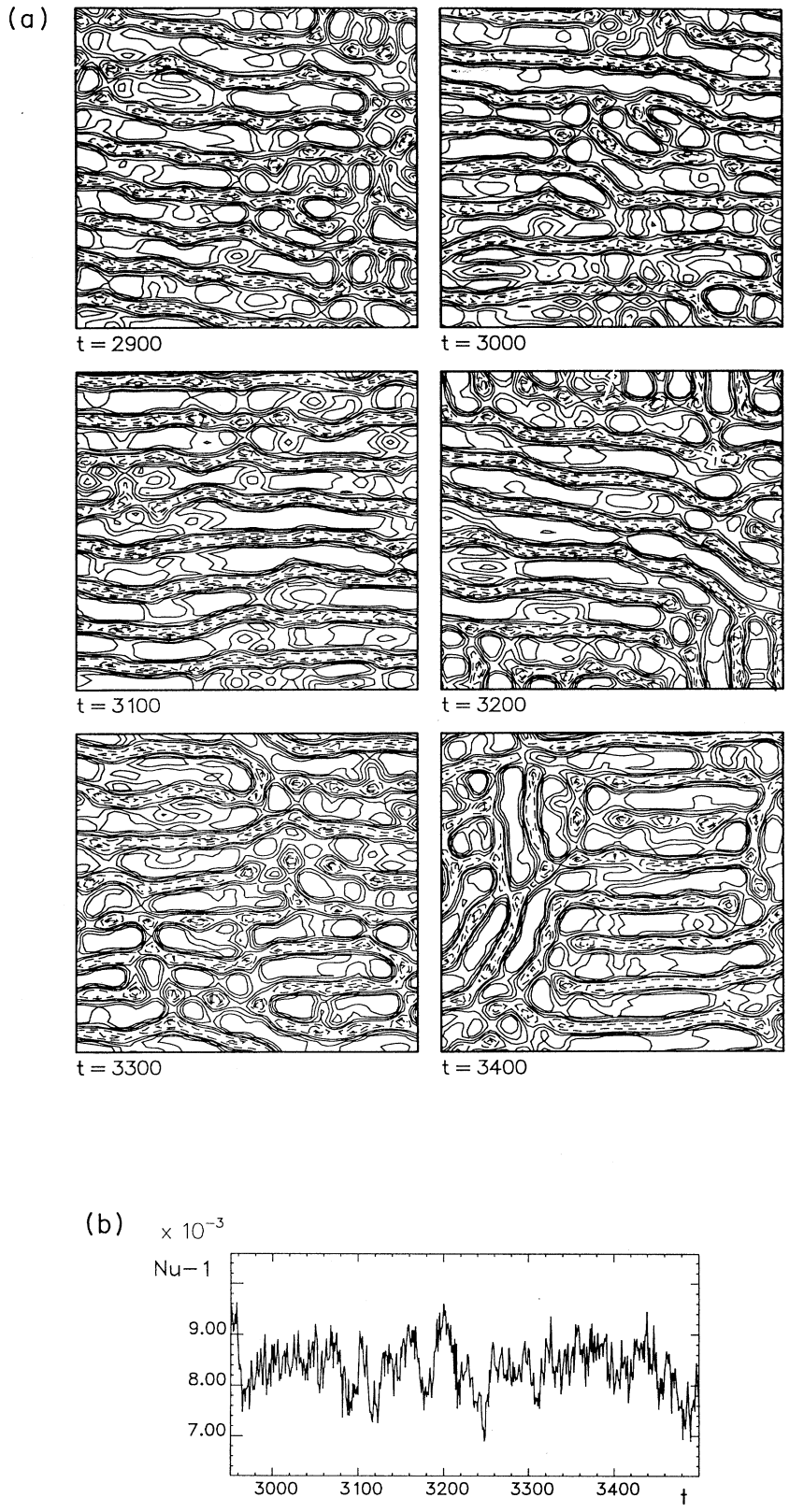

FIG. 9. Weak turbulence in Bénard-Marangoni convection at low Prandtl number. (a) Surface temperature field evolving from a random initial condition for Pr=0.5, ε=0.5, Bi=0.1. Parallel rolls are unstable due to a skewed varicose instability. (b) Reduced Nusselt number Nu(t)−1 according to Eq. (23). No stationary state is obtained.

the g hexagon. Thus, the intensification of kinetic energy production by expansion of the energy-producing temperature gradient constitutes the reason for the preference of l hexagons in high-Prandtl-number convection. Incidentally, we have obtained a perfect lattice of g hexagons in an infinite-Prandtl-number simulation after we had artificially changed the sign of the nonlinear term in the heat equation (3).

Now we turn to the case of low-Prandtl-number fluids, which can be also understood by the selection principle formulated above. First we note that the quantity that is advected by the dominant nonlinear effects is now the vorticity, not the temperature, since the temperature field is governed by the linear equation (7b), and the only nonlinear term comes from the Navier-Stokes equation. The initial vorticity distribution [Fig. 8(a)] is redistributed in such a way [Fig. 8(b)] that the vorticity concentrates above the cold regions and forms an intense cold jet directed away from the free surface. The jet is seen in Fig. 8(c), in which we have plotted the averaged vertical velocity obtained from a direct numerical simulation of the zero-Prandtl-number model at $\mathrm{Ma}=100$ and $\mathrm{Bi}=0$. How does this nonlinear effect modify the kinetic energy production in a circular cell when the fluid is flowing upward or downward in the center of the cell? As in the previous case, this question shall be answered by rewriting the energy production integral in cylindrical coordinates, however, in terms of the vertical velocity. Denoting the typical vertical bulk velocity by $\bar{v}_z(r)$ and assuming a large cell aspect ratio ($\partial_x \ll 1, \partial_y \ll 1, \partial_z \sim 1$), we can derive the relation $\theta \sim \bar{v}_z$ from Eq. (7b). Using $\partial_r(rv_r) \sim \bar{v}_z$, which follows from the continuity equation (2) and performing a partial integration in Eq. (19), yields the estimate

$$\int \left[\frac{\bar{v}_z^2}{r} \right] r \, dr \tag{22}$$

for the thermocapillary energy production in fluids with $\mathrm{Pr} \ll 1$. The integral is deliberately written in a form that highlights the difference from the total kinetic energy $\int \bar{v}_z^2 r \, dr$, which lacks the weight factor $1/r$. From the presence of this factor in (22) it follows that the production of kinetic energy in low-Prandtl-number convection is intensified by those isoenergetic redistributions of vorticity that lead to a concentration of the vertical velocity in the vicinity of the center of the cell. This explains the dominance of g hexagons in low-Prandtl-number Bénard-Marangoni convection.

VI. CONCLUSIONS AND OUTLOOK

We have predicted that Bénard-Marangoni convection sets in as a pattern of g hexagons if the Prandtl number of the fluid is less than $\mathrm{Pr}_c \approx 0.22$. Although the experimental study of low-Prandtl-number BMC is a highly complex task since liquid metals at low temperature are prone to surface oxidation (Ginde, Gill, and Verhoeven [8], Bojarevics, Gelfgat, and Gerbeth [19]) new experimental studies are likely to appear in the foreseeable future. As the free surface is convex over the center of a g hexagon (and concave over an l hexagon) optical methods should be capable of distinguishing between these two types of hexagons, thereby testing the correctness of our theoretical prediction.

Though our study is focused on the weakly nonlinear regime of BMC, we wish to mention that the stationary structures summarized in the state diagram of Fig. 6 become time dependent at comparatively low values of ε. In the following we provide a first glimpse at the time-dependent and possibly turbulent phenomena in low-Prandtl-number BMC that are currently being investigated in detail.

Amplitude equations of the form (12) are derived by elimination of the enslaved variables [20]. For very small Pr, the toroidal part of the velocity will not longer follow the poloidal part adiabatically and may account for another order parameter, leading eventually to a weakly turbulent behavior that characterizes pattern formation in the low-Prandtl-number regime if non-Boussinesq terms are absent [21]. This order parameter has a large-scale spatial structure and is therefore suppressed in a small-aspect-ratio system. From our direct numerical simulations for large aspect ratio we found that for larger ε and small Pr, a zone inside the parabola (18) occurs where the rolls are unstable to a secondary instability (skewed varicose) rendering the structure time dependent and leading eventually to a weakly turbulent spatiotemporal behavior, as shown Fig. 9(a) where we show the evolution of surface temperature in the time-dependent regime. This instability is in qualitative agreement with previous results for rigid boundary conditions on the top and bottom of the layer [21] and was first predicted by Siggia and Zippelius [22] due to the coupling of the large-scale vorticity to the small-scale temperature field.

To demonstrate the intrinsic time dependence of the pattern, we computed the Nusselt number that measures the heat flux through the layer in the vertical direction:

$$\mathrm{Nu}(t) = 1 - \langle \partial_z \theta(\mathbf{x}, t)|_{z=0} \rangle_{x,y} \, , \tag{23}$$

where $\langle \, \rangle_{x,y}$ denotes the average over the horizontal coordinates (see, e.g., [23]). The temporal evolution of the Nusselt number corresponding to the series presented in Fig. 9(a) is shown in Fig. 9(b). It is obvious that the pattern will not settle down to a stationary solution but rather stays time dependent forever.

ACKNOWLEDGMENTS

The authors are grateful to G. Lebon for making available the manuscript [13] prior to publication. Furthermore, we thank K. Nitschke and C. Pérez-Garcia for helpful discussions. This work was partially supported by the Deutsche Forschungsgemeinschaft under Grants No. Th 497/2-1 and No. Th 497/9-1. One of us (A.T.) is grateful to S. A. Orszag for his hospitality during a stay at Princeton University, where the infinite-Prandtl-number computations have been performed.

[1] H. Bénard, Rev. Gén. Sci. Pures Appl. **11**, 1261 (1900).
[2] M. J. Block, Nature **178**, 650 (1956).
[3] J. R. Pearson, J. Fluid Mech. **4**, 489 (1958); D. Nield, *ibid.* **19**, 341 (1964).
[4] E. L. Koschmieder and D. W. Switzer, J. Fluid Mech. **240**, 533 (1992), and references therein.
[5] P. Cerisier, P. Perez-Garcia, and R. Occelli, Phys. Rev. E **47**, 3316 (1993), and references therein.
[6] M. Bestehorn, Phys. Rev. E **48**, 3622 (1993).
[7] A. Thess and S. A. Orszag, J. Fluid Mech. **283**, 201 (1995).
[8] R. Ginde, W. N. Gill, and J. D. Verhoeven, Chem. Eng. Commun. **82**, 223 (1989).
[9] S. Rosenblat, S. H. Davis, and G. M. Homsy, J. Fluid Mech. **120**, 91 (1982).
[10] P. C. Dauby, G. Lebon, P. Colinet, and J. C. Legros, Q. J. Mech. Appl. Math. **46**, 683 (1993).
[11] α is the heat transfer coefficient at the free surface and λ is the heat conductivity of the fluid. Equation (5b) derives from the phenomenological boundary condition $\lambda\partial_z T=-\alpha(T-T_0)$ sometimes called "Newton's law of cooling."
[12] S. H. Davis, Ann. Rev. Fluid Mech. **19**, 403 (1987).
[13] P. M. Parmentier, V. C. Regnier, and G. Lebon (unpublished).
[14] O. Thual, J. Fluid Mech. **240**, 229 (1992).
[15] L. Landau and E. M. Lifshitz, *Course of Theoretical Physics,* Fluid Mechanics, Vol. 6 (Pergamon, New York, 1987).
[16] F. Busse, Rep. Prog. Phys. **41**, 1929 (1978).
[17] L. A. Segel, J. Fluid Mech. **19**, 203 (1969).
[18] M. Bestehorn and C. Pérez-García, Europhys. Lett. **4**, 1365 (1987).
[19] A. Bojarevics, Y. M. Gelfgat, and G. Gerbeth, in "Magnetohydrodynamics," Plenum, New York, (in press).
[20] H. Haken, *Synergetics* (Springer-Verlag, Berlin, 1983).
[21] F. H. Busse and R. M. Clever, J. Fluid Mech. **91**, 319 (1979).
[22] E. D. Siggia and A. Zippelius, Phys. Rev. Lett. **4**, 1365 (1987).
[23] J. K. Platten and J. C. Legros, *Convection in Liquids* (Springer-Verlag, Berlin, 1984).